Efficient Real Gas Upwinded Navier-Stokes Computations of High Speed Flows

William J. Coirier*

NASA Lewis Research Center, Cleveland, Ohio 44135

An efficient method to account for the chemically frozen thermodynamic and transport properties of air in three-dimensional Navier-Stokes calculations has been demonstrated. This approach uses an explicitly specified equation of state (EOS) so that the fluid pressure, temperature, and transport properties are directly related to the flow variables. The method is efficient since no subiterations are required to deduce the pressure and temperature from the flux variables and is modular by allowing different equations of state to be easily supplied to the code. The flexibility of the EOS approach is shown by its implementation into a high-order total variation diminishing upwinding scheme as well as a standard central-differencing scheme. The EOS approach is then demonstrated by computing the hypersonic flow through the corner region of two mutually perpendicular flat plates using both the upwind and central-differencing schemes.

Introduction

THE capability to efficiently compute chemically frozen single-stream flows using an explicitly specified equation of state (EOS) has been added to a three-dimensional Navier-Stokes solver. This flow solver is based upon the PARC codes, whose origin can be traced to the AIR2D/3D solvers by Pulliam and Steger,[1] which used the block alternating direction implicit (ADI) algorithm presented by Beam and Warming.[2] To increase the computational efficiency and to reduce storage requirements, Pulliam[3] diagonalized the block implicit operators of the original Beam-Warming ADI algorithm, resulting in the ARC2D/3D codes. Cooper[4] further modified the ARC codes to be used in a production environment for solving the propulsion-oriented applications at the Arnold Engineering Development Center, resulting in the PARC codes. Coirier[5] replaced the implicit operator with the LU-SGS (lower-upper symmetric Gauss-Seidel) algorithm and demonstrated this scheme for hypersonic corner and gap-seal problems. This scheme is based on an LU decomposition method proposed by Jameson and Turkel[6] and demonstrated by Jameson and Yoon[7] for the Euler equations. In addition, Shuen and Yoon[8] and Yu et al.,[9] with the RPLUS series of codes, have shown the efficiency and robustness of this algorithm for solving the Navier-Stokes equations fully coupled to the chemical transport equations for computing finite-rate chemically reacting flowfields.

For flows where the dissociation and recombination rates are much slower than the fluid residence time (i.e., in the limit as the Damkohler number approaches zero), the fluid can be modeled as a mixture of inert (chemically frozen) gases. When the converse is true (i.e., the Damkohler number approaches infinity), the fluid can be modeled as if it were in chemical equilibrium. If either of these limitations holds for the flowfield to be considered, great simplifications can be made and the resulting computational work reduced. The present research demonstrates the capability to efficiently model gen-

eral, nonmixing, chemically frozen flows using a method based on a generalized equation of state. An EOS for chemically frozen air is generated, and its ease in implementation is shown for both a high-order total variation diminishing (TVD) upwinding scheme (based upon flux differencing[10] and Van Leer's flux vector splitting[11]) as well as a standard central-differencing scheme with added first and third difference dissipation. The upwinding scheme is then compared favorably to experimental data for the hypersonic flow through the corner region of two mutually perpendicular flat plates (corner flow). To demonstrate the EOS, a similar corner flowfield is computed at a higher freestream stagnation enthalpy, and detailed comparisons between the central difference and upwinding schemes are made for both $\gamma = $ const and the chemically frozen air EOS.

Equation of State Formulation

To account for variable thermodynamic and transport properties, it is necessary to relate the pressure, temperature, and transport properties to the flow variables. In the majority of flow solvers, the fluid specific heats are assumed to be constant, resulting in a simple equation of state, namely,

$$p = (\gamma - 1)\rho e \qquad (1)$$

$$T = \frac{p}{\rho R} \qquad (2)$$

$$\gamma = \frac{C_p}{C_v} \qquad (3)$$

The speed of sound is then easily found, under the assumption of thermal equilibrium, as

$$a^2 \equiv \left(\frac{\partial p}{\partial \rho}\right)_s = \frac{\partial p}{\partial \rho} + \frac{p}{\rho^2}\frac{\partial p}{\partial e} \qquad (4)$$

$$a^2 = \gamma\frac{p}{\rho} \qquad (5)$$

For high enthalpy flows, the assumption of constant γ can lead to overpredictions of the temperatures and pressures near stagnation conditions. Real gas effects for compressible flow calculations have been made by many researchers for mixing and nonmixing flows that are considered to be chemically frozen or in chemical equilibrium or nonequilibrium.[8,9,12,13] For the frozen and finite-rate approaches, once the chemical composition is known, the pressure and temperature are

*Aerospace Engineer, Computational Fluid Dynamics Branch. Member AIAA.

found in much the same manner. The mixture enthalpy is formed based on the chemical composition and the individual species enthalpy as

$$h(T) = \sum_{i=1}^{N} Y_i h_i \tag{6}$$

where the $h_i(T)$ are typically in the form of polynomials in temperature. This is then related to the internal energy (which is readily obtained from the flux variables) by assuming the fluid is ideal, so that

$$e = h(T) - \frac{p}{\rho} \tag{7}$$

Then the temperature is found by solving Eq. (7) for T (typically by Newton's iteration) and the pressure is found from Eq. (2). This approach allows mixing or nonmixing chemically frozen flows to be calculated in a finite-rate chemistry code by simply switching off the chemical source terms or the species equations completely, but it loses efficiency by having to perform the temperature inversion subiterations at each grid point for each global iteration level. Not only is more work required to perform these subiterations, but also the existence of subroutine calls in the do-loop structure can devectorize computationally intensive portions of the code (e.g., pressure terms in the inviscid flux vectors for the residual calculations). Naturally, one could restructure the code in a vectorizable fashion to perform the enthalpy inversion in Eq. (7) and then store the pressure and temperature at each grid point. But this would require storing the pressure and temperature in main memory and would require extensive revision to the flow solver's structure. By having an explicit relationship between the pressure, temperature, and flux variables, significant savings in work and memory can be achieved by eliminating the enthalpy/temperature inversion subiterations and subroutine calls and the need to store pressure and temperature at each grid point.

Recent work by Shuen and Liou[14] and Liou et al.[15] in developing flux-splitting methods for real gases has made use of an explicitly specified EOS. This concept was successfully applied by Liou[16] for real gas calculations of a corner flow-field using a parabolized Navier-Stokes code. By having an explicitly specified EOS, advantages in flexibility and efficiency for frozen and equilibrium flows are apparent. No "effective γ" approximations need to be made in forming flux Jacobians and no subiteration procedure is needed to find the pressure and temperature. In addition, the real gas flux-splitting methods in Refs. 15 and 16 can be extended to the code once the generalized EOS is operational.

The EOSs generated for this work use thermodynamic and transport data from the NASA Lewis Chemical Equilibrium program, CEC.[17] This program accesses an extensive data bank that contains thermodynamic data (in the form of polynomials in temperature for individual species' specific heats, enthalpy, and Gibb's energy) for 741 gaseous species, and transport property data (in the form of polynomials in temperature for individual species' molecular viscosities and thermal conductivities) for 154 gaseous species. For mixtures in chemical equilibrium, it uses a Gibb's energy minimization procedure that is fully outlined in Ref. 17. Considering the large amount of thermodynamic and transport data contained in the aforementioned data banks, a wide variety of different gaseous mixtures can be simulated using the EOS approach.

The chemically frozen EOSs generated here are made using a least squares surface fit that minimizes the relative error between the fit function and the supplied data. Given the chemical composition, Y_i, the internal energy and density are computed over a wide range of pressures and temperatures using the thermodynamic data in Ref. 17. Then $p(\rho,e)$ and $T(\rho,e)$ are found by applying the surface-fitting procedure. Individual species' transport properties are calculated from Ref. 18, from which the mixture properties are found using

the Wilke mixing rule. The fits for the mixture laminar viscosity and thermal conductivities are then made from this data set.

Now that $p(\rho,e)$ and $T(\rho,e)$ are known, the derivatives $\partial p/\partial \rho$ and $\partial p/\partial e$ can be analytically found. By explicitly knowing the pressure derivatives, no additional approximations need to be made in forming the flux Jacobians. In addition, when forming the inviscid flux vectors, the pressure is immediately available from an evaluation of the equation of state. The EOS fits are formulated as statement functions used by the code and are contained in FORTRAN include files. This allows different EOS functions to be easily supplied to the code. By having the EOSs as statement functions, the original vectorization structure is unaffected and no subiterations or extra memory are required to obtain the pressure and temperature. With this approach, a previously written, non-real gas code can be modified in a straightforward manner to include the real gas effects, while still maintaining its original structure and efficiency.

Chemically Frozen Air Equation of State

The procedure outlined in the previous section has been used to generate an equation of state for air under the assumption that the fluid is ideal and its composition remains chemically frozen. The mole fraction composition of air is taken to be $X_{N_2} = 0.78847$ and $X_{O_2} = 0.21153$, which is used in conjunction with the thermodynamic data from CEC to generate the density and internal energy over an extremely wide pressure and temperature range. The CEC data for enthalpy used to generate the pressure/temperature map has been calculated by statistical mechanics over the temperature range of $200 < T < 15,000$ K.[19] Since the surface-fitting procedure used in the generation of the EOS will have the largest errors near the boundaries of the domain, an extremely wide pressure and temperature range was used to compute the density and internal energy. The density and internal energy were computed given the pressure and temperature over the range of $1.0 \times 10^{-4} < P < 100.0$ atm and $20 < T < 15,000$ K. (For $T < 200$ K, the specific heats are assumed to be equal to their values at $T = 200$.) Great care was taken in choosing the surface-fitting base functions to keep a high level of fitting accuracy over the entire fitting range. The root mean square of the relative error for the pressure, temperature, laminar viscosity, and thermal conductivity fits was, respectively, 0.42, 0.34, 1.7, and 1.2%. The Appendix contains the surface-fitted base functions and coefficients for the fits of pressure, temperature, laminar viscosity, and thermal conductivities. For comparative purposes, an EOS for calorically perfect air was also generated following Eqs. (1), (2), and (5) using $\gamma = 1.4$.

Comparisons between the calorically perfect and thermally perfect equations of state in terms of pressure, temperature, laminar viscosity, and thermal conductivity are made in Figs. 1 and 2. The comparison of pressures, in Fig. 1a, shows that the deviation of the calorically perfect from the thermally perfect gas assumption is small, but not negligible, while the temperature differences, in Fig. 1b, can be quite significant in the higher internal energy range. The comparisons of laminar viscosity and thermal conductivity, in Figs. 2a and 2b, show that the thermally perfect formulations follow the NBS standards[20] more closely than the calorically perfect formulations. For the calorically perfect transport properties, Sutherland's law is used for the laminar viscosity, while the thermal conductivity formulation assumes constant specific heats and Prandtl number ($P_r = 0.72$) and uses Sutherland's law for the laminar viscosity.

Numerical Solution Procedure

The flow solver used in this study solves the Navier-Stokes equations cast in divergence form evaluated in a generalized curvilinear coordinate system. The equations are solved implicitly using the LU-SGS algorithm for approximate Newton
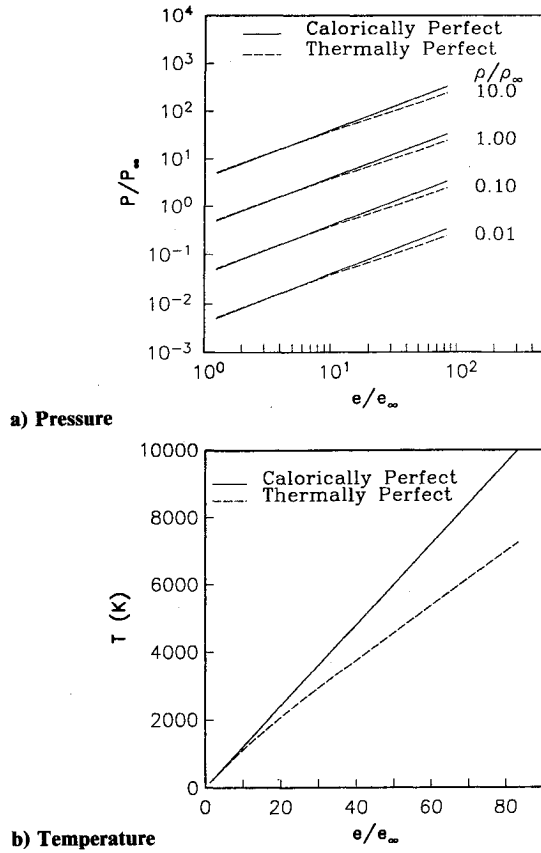
a) Pressure

b) Temperature

Fig. 1 Equation of state comparisons.

a) Laminar viscosity

b) Thermal conductivity

Fig. 2 Equation of state comparisons.

iteration and are discretized in a finite difference formulation. The original discretization of the convective terms is central differencing with added first and third difference dissipation. The coefficients controlling the levels of dissipation are kept at their default levels ($\kappa_2 = 0.25$ and $\kappa_4 = 0.01$) for all of the computations performed here. A complete discussion of the central-difference discretization scheme and the type of numerical dissipation are available in the literature.[1-4] To aid in the shock-capturing ability of the code, a second-order TVD upwinding scheme based on flux differencing[10] and Van Leer's flux vector splitting[11] has been implemented using the generalized equation of state formulation. The following sections briefly describe the implicit and explicit portions of the solution scheme and show how the generalized equation of state is implemented.

LU-SGS Algorithm

The LU-SGS scheme was first demonstrated by Yoon and Jameson[21,22] in solving the Euler and Navier-Stokes equations. For computing flows with finite-rate chemistry, this scheme has been shown to be very efficient by implicitly solving the Navier-Stokes equations fully coupled to the chemical transport equations.[8,9,23] For solving the Euler or Navier-Stokes equations alone, the resulting scheme is scalar diagonal and requires only two sweeps with scalar inversions for both two- and three-dimensional problems. When point source terms are included implicitly, the approach results in block diagonal operators. Following the procedure outlined in Ref. 5, the hybrid LU-SGS scheme can be derived from the following.

A general scheme for solving the Navier-Stokes equations in delta form by implicitly including the inviscid terms may be written as

$$[I + \Delta t(D_\xi A + D_\eta B + D_\zeta C)]\Delta q = - \Delta tR \qquad (8)$$

where R, the residual, is the discrete representation of the steady terms in the Navier-Stokes equations, D_ξ, D_η, and D_ζ
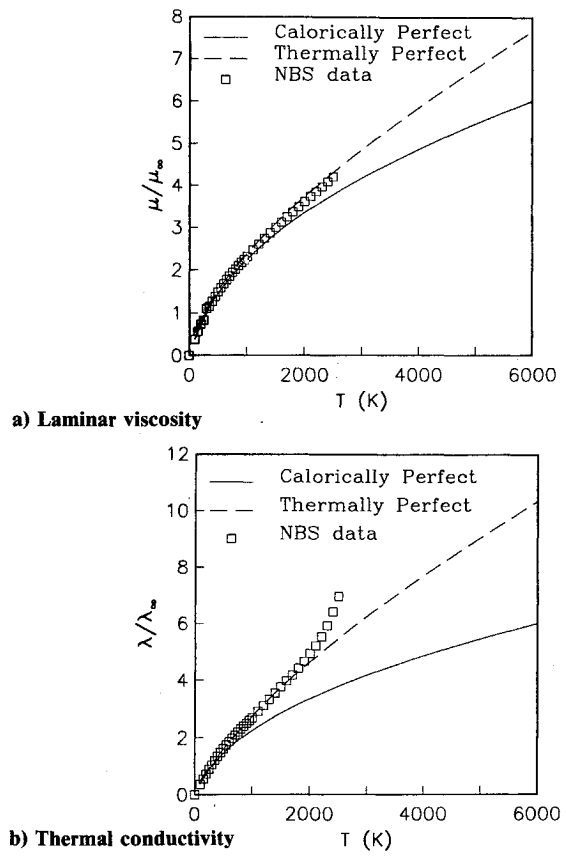
are difference operators that approximate ∂_ξ, ∂_η, and ∂_ζ, and A, B, and C are the inviscid flux Jacobians

$$A = \frac{\partial E}{\partial q}, \qquad B = \frac{\partial F}{\partial q}, \qquad C = \frac{\partial G}{\partial q} \qquad (9)$$

If the flux Jacobians in Eq. (8) are conditioned so that they can be split into " + " and " − " matrices, where the eigenvalues of the + matrices are non-negative and the eigenvalues of the − matrices are nonpositive, and then upwind differenced according to their sign, Eq. (8) may be written as

$$[I + \Delta t(\nabla_\xi A^+ + \Delta_\xi A^- + \nabla_\eta B^+ + \Delta_\eta B^- + \nabla_\zeta C^+$$

$$+ \Delta_\zeta C^-)] = - \Delta tR \qquad (10)$$

The choice of conditioning used to form the approximated Jacobians is very important, and following the construction used in Ref. 24, the approximated Jacobians are formed as

$$A^\pm = \frac{A \pm r_A I}{2}, \qquad B^\pm = \frac{B \pm r_B I}{2}, \qquad C^\pm \frac{C \pm r_C I}{2} \qquad (11)$$

where

$$r_{A,B,C} = \beta \, \max(|\lambda_{A,B,C}|) \qquad (12)$$

where $\beta \geq 1.0$ and $\lambda_{A,B,C}$ are the eigenvalues of the flux Jacobians. Therefore, using the conditioning in Eq. (11), the unfactored scheme may be written as

$$\{I[1 + \Delta t(r_A + r_B + r_C)]$$

$$+ \Delta t(A_{j-1}^- + B_{k+1}^- + C_{l-1}^- - A_{j-1}^+ - B_{k-1}^+ - C_{l-1}^+)\}\Delta q$$

$$= - \Delta tR \qquad (13)$$

where (j,k,l) refers to the grid point index. (When an index is omitted, it is assumed to be at j, k, or l.) The hybrid LU-SGS scheme for approximate Newton iteration is found by dividing Eq. (13) by Δt and taking the limit as Δt approaches ∞ and factoring the resulting operator into L, D, and U operators. The D operator is scalar diagonal, so after moving this to the right-hand side, the hybrid LU-SGS scheme for approximate Newton iteration may be written as

$$LU\Delta q = -(r_A + r_B + r_C)R \qquad (14)$$

$$L = [I(r_A + r_B + r_C) - A_{j-1}^{\pm} - B_{k-1}^{\pm} - C_{l-1}^{\pm}] \qquad (15)$$

$$U = [I(r_A + r_B + r_C) + A_{j+1}^{-} + B_{k+1}^{-} + C_{l+1}^{-}] \qquad (16)$$

The solution of Eq. (14) is fully vectorizable on planes where $j + k + l = \text{const}$ and is efficient since it requires only scalar diagonal inversions. The approach is to first solve for an intermediate vector using Eq. (15) by sweeping in the direction of planes of increasing $j + k + l$ and then solve for Δq using Eq. (16) by sweeping in the opposite direction. One advantage of the approximate Newton iteration form is that no choice of Courant number is needed. Since an optimal Courant number is very seldom known a priori, the scheme can yield converged solutions faster than the diagonalized Beam-Warming scheme (which was originally present in the code). Results in Ref. 5 show that the scheme is more efficient in processing time per iteration than the diagonalized Beam-Warming scheme and, for the test cases in the report, indicate that the LU-SGS scheme for approximate Newton iteration converged faster than the Beam-Warming scheme.

The inclusion of the generalized equation of state formulation in the LU-SGS scheme is straightforward. Since the pressure derivatives $\partial p/\partial \rho$ and $\partial p/\partial e$ are directly obtainable from the EOS formulation, the inviscid flux Jacobians can be found with no "equivalent gamma" assumptions. Therefore, the only modifications to the LU-SGS scheme using the generalized equation of state formulation is to include the general pressure formulation and its derivatives in the inviscid flux Jacobians A, B, and C in Eqs. (14–16) as well as the speed of sound definition in Eq. (4). A general inviscid flux vector and its Jacobian, including the pressure derivative terms, is shown in Ref. 28.

Upwinding Approach

The upwinding approach used here is based upon flux differencing[10] and Van Leer's flux vector splitting method.[11] The upwinding approach in Ref. 10 uses a monotone interpolation of the non-normalized, nodal point, split inviscid fluxes to cell interfaces using a variable order polynomial interpolation scheme. The numerical fluxes evaluated at the cell interfaces consist of the upwind components and are written as

$$\tilde{F}_{i+\frac{1}{2}} = \tilde{F}_{i+\frac{1}{2}}^{+} + \tilde{F}_{i+\frac{1}{2}}^{-} \qquad (17)$$

The interpolation used here interpolates cell face normalized fluxes, simplifying somewhat the approach presented in Ref. 10. For the "positive" flux contributions, the normalized cell interface flux is monotonically interpolated from the nodal values as

$$\tilde{F}_{i+\frac{1}{2}}^{+} = F_i^{+} + \delta_i^{+} \qquad (18a)$$

$$\tilde{F}_{i+\frac{1}{2}}^{-} = F_{i+1}^{-} - \delta_{i+1}^{-} \qquad (18b)$$

where

$$\delta_i^{+} = C_1^{+} \Delta^{-} F_i^{+} + C_2^{+} \Delta^{+} F_i^{+} \qquad (19a)$$

$$\delta_i^{-} = C_1^{-} \Delta^{+} F_i^{-} + C_2^{-} \Delta^{-} F_i^{-} \qquad (19b)$$

The order of the interpolation scheme and its limiting are contained in the coefficients $C_{1,2}^{\pm}$, which are written as

$$C_1^{+} = \phi(r_i^{+})\left[\frac{\theta}{4}\left(1 - \kappa - \frac{\sigma}{2}\right)\right] \qquad (20a)$$

$$C_2^{+} = \phi\left(\frac{1}{r_i^{+}}\right)\left[\frac{\theta}{4}\left(1 + \kappa + \frac{\sigma}{2}\right)\right] \qquad (20b)$$

$$C_1^{-} = \phi(r_i^{-})\left[\frac{\theta}{4}\left(1 - \kappa + \frac{\sigma}{2}\right)\right] \qquad (20c)$$

$$C_2^{-} = \phi\left(\frac{1}{r_i^{-}}\right)\left[\frac{\theta}{4}\left(1 + \kappa - \frac{\sigma}{2}\right)\right] \qquad (20d)$$

The limiters in Eqs. (20) are formed based on the inner products of neighboring flux differences. Although this approach does not strictly adhere to the traditional method of limiting each flux individually, it has been stated to be satisfactory over a sufficiently wide range of conditions.[10] The limiter arguments $r_i^{\pm}$ are written as

$$r_i^{+} = \frac{\Delta^{+} F_i^{+} \circ \Delta^{-} F_i^{+}}{\Delta^{-} F_i^{+} \circ \Delta^{-} F_i^{+}} \qquad (21a)$$

$$r_i^{-} = \frac{\Delta^{+} F_i^{-} \circ \Delta^{-} F_i^{-}}{\Delta^{+} F_i^{-} \circ \Delta^{+} F_i^{+}} \qquad (21b)$$

The limiter function is taken to be the minimum-modulus (min-mod) function, where

$$\phi(r) = \max[0.0, \min(r, 1.0)] \qquad (22)$$

The variables κ, σ, and θ set the order of the scheme. For all of the following upwinded calculations, second-order, full upwinding is used so that $\kappa = -1.0$, $\sigma = 0.0$, and $\theta = 1.0$. Combining the positive and negative fluxes, the cell face normalized numerical flux is then represented as

$$\tilde{F}_{i+\frac{1}{2}} = \frac{1}{2}(F_i + F_{i+1}) - \frac{1}{2}\Delta^{+}(F_i^{+} - F_i^{-}) + (\delta_i^{+} - \delta_{i+1}^{-}) \qquad (23)$$

The first term represents a simple numerical average of the nodal fluxes whereas the combination of the first and second terms results in a first-order upwinding scheme. The third terms represent antidiffusive fluxes that increase the order of accuracy of the scheme and are limited to make the scheme monotone.

After the construction of the numerical fluxes at the cell interfaces, the convective contribution to the residual from this coordinate direction is then calculated as

$$R_i = (\tilde{F}\delta)_{i+\frac{1}{2}} - (\tilde{F}\delta)_{i-\frac{1}{2}} \qquad (24)$$

where δ is the cell interface area. The areas and projected areas at the cell interfaces are found using the transformation metrics evaluated at the nodal points in a consistent manner as (for the ξ flux)

$$(\delta_x)_{i+\frac{1}{2}} = \frac{1}{2}[(\xi_x/J)_i + (\xi_x/J)_{i+1}] \qquad (25a)$$

$$(\delta_y)_{i+\frac{1}{2}} = \frac{1}{2}[(\xi_y/J)_i + (\xi_y/J)_{i+1}] \qquad (25b)$$

$$(\delta_z)_{i+\frac{1}{2}} = \frac{1}{2}[(\xi_z/J)_i + (\xi_z/J)_{i+1}] \qquad (25c)$$

so that the cell interface area is

$$\delta = \sqrt{\delta_x^2 + \delta_y^2 + \delta_z^2} \qquad (26)$$

Since this scheme operates only on flux differences, it is possible to use either a flux vector splitting approach or a flux difference splitting approach. Van Leer's flux vector splitting was chosen due to its simplicity and efficiency and for the ease in which the generalized equation of state could be included. It should be noted that the equation of state formulation does not preclude the use of Roe's flux difference splitting approach, which would include the explicitly specified pressure derivatives $\partial p/\partial \rho$ and $\partial p/\partial e$ in the formulation of the transformation matrices, as in Ref. 15. The flux vector splitting used here is formulated, including the pressure and sound speed, to facilitate using the generalized EOS, so that when $|\tilde{M}_c| \leq 1.0$

$$
F^{\pm} = \left\{ \begin{array}{c} \pm \dfrac{\rho a}{4} (\tilde{M}_c \pm 1)^2 \\[2mm] F_1^{\pm} \left[u - \dfrac{\delta_x}{\delta} \dfrac{P}{\rho a^2} (\mp 2a + \tilde{u}_c) \right] \\[2mm] F_1^{\pm} \left[v - \dfrac{\delta_y}{\delta} \dfrac{P}{\rho a^2} (\mp 2a + \tilde{u}_c) \right] \\[2mm] F_1^{\pm} \left[w - \dfrac{\delta_z}{\delta} \dfrac{P}{\rho a^2} (\mp 2a + \tilde{u}_c) \right] \\[2mm] F_1^{\pm} [H - m (\tilde{u}_c \mp a)^2] \end{array} \right\} \quad (27)
$$

and when

$$\tilde{M}_c > 1.0: \quad F^+ = F, \quad F^- = 0 \quad (28a)$$

$$\tilde{M}_c < 1.0: \quad F^+ = 0, \quad F^- = F \quad (28b)$$

where the contravariant velocity and Mach number are defined in terms of the areas and projected areas at the cell interfaces. The parameter m in Eq. (27) is found by requiring the bracketed terms in the energy flux to form a perfect square, which is then modified so that an indeterminate expression is avoided at stagnation points and no-slip boundaries, resulting in the original one-dimensional form of m

$$m = \frac{(h/a^2)}{1 + 2(h/a^2)} \quad (29)$$

The inclusion of the generalized equation of state formulation into this upwinding scheme is straightforward. At each nodal point, the flux variables directly yield ρ and e, which in turn give p and a^2 directly from the equation of state from which the flux vector in Eq. (27) is constructed. The inclusion of the EOS into the central-differencing scheme is also straightforward; the inviscid flux vectors are constructed using the pressure evaluated from the EOS, and the spectral radii (needed for the artificial dissipation) are computed using the sound speed from the EOS. This approach using the generalized equation of state requires no special subiterations or procedures to find the pressure, temperature, sound speed, or static enthalpy and allows the upwinding approach to be fully vectorized. It should be noted that the original code structure is identical, and only a minimum of work was required to add the EOS capability. In addition, as the following sections note, the efficiency of the solver is only marginally degraded to include the real gas effects.

Corner and Gap Seal Flowfield Study

Effort is currently under way to investigate the heat transfer and aerodynamic loads in and around a scramjet module gap seal configuration.[5,28] The seal system must prevent high temperature and pressure gases from leaking through the gap between the articulating engine panel walls and stationary splitter panels.[25] This system is crucial to the design of hypersonic airbreathing propulsion systems and presents a significant challenge to structural designers to build a viable seal system. To assist the design effort, the present research complements the structural analysis under way in an attempt to better understand the fluid dynamic and heat transfer phenomena in and around the gap seal system. The addition of real gas effects and the inclusion of a high-order TVD upwinding scheme are motivated by this effort since a more thorough understanding of the underlying fluid dynamic process can help the design effort.

Hypersonic Corner Validation

To obtain some level of confidence in the modeling of the gap seal flow, the three-dimensional Navier-Stokes solver has been validated[5] against experimental data taken from a class of flows similar to the gap seal flow. The gap seal geometry is similar to two mutually perpendicular flat plates (corner) aligned with the freestream flow with a "groove" situated at the plate intersections. Due to this similarity, the three-dimensional code was validated against the experimental data of hypersonic corner flow taken by Cresci.[26] These tests were conducted at a Mach number of 11.8 over a range of Reynolds numbers of 0.15×10^6 to 0.5×10^6 per foot. The data presented in Refs. 5 and 26 are axial pressures and heat transfer rates plotted against the hypersonic interaction parameter

$$\chi = \frac{c^{1/2} M_\infty^3}{Re_x^{1/2}} \quad (30)$$

for different lateral locations measured from the corner. In addition, surface pressures, heat transfer rates, and skin friction data comparisons were made as a function of lateral distance from the corner at various axial locations. This data not only tests the prediction of the mutual interaction of the two plate boundary layers on each other but also the self-induced leading-edge pressures caused by the boundary-layer growth close to the leading edges.

A complete set of comparisons are favorably made against this set of experimental data using the central-differencing scheme in Ref. 5. The same flowfield was also computed using the second-order TVD upwinding scheme outlined in the present paper, and limited comparisons to the experimental data are made here. Since the stagnation temperature was low ($T_{st,\infty} = 944$ K), the generalized equation of state was not used, so that in essence, this validation effort tests the upwinding approach. A relatively coarse grid ($36 \times 41 \times 41$) was used for plate lengths and widths of 8 and 2.5 in., respectively. The Reynolds number per foot was taken to be 0.15×10^6, resulting in a Reynolds number based on plate length of 1.0×10^5 from which the flow is assumed to be laminar. The grids were clustered normally in the cross-stream planes using a Robert's transformation with $\beta = 1.01$ and axially near the leading edge using $\beta = 1.1$, with five grid points extended ahead of the leading edge.

The comparisons to experiment of the upwind computation were nearly identical to the central-difference results. Since the central-difference results already computed and shown in Ref. 5 were favorable, and the upwinded results computed here were nearly the same, only a selected portion of the comparisons to experiment are shown here. Figure 3a shows the predicted wall pressures vs the hypersonic interaction parameter at a station 0.125 in. away from the corner intersection, whereas Fig. 3b compares the computed and measured lateral variation of heat transfer at a location of $\chi = 8.3$. As can be seen from this figure, the upwinding approach correctly simulates the mutual interaction of the plate boundary layers and the lateral variation of the heat transfer to the plates caused by the leading-edge shock and boundary-layer interaction.
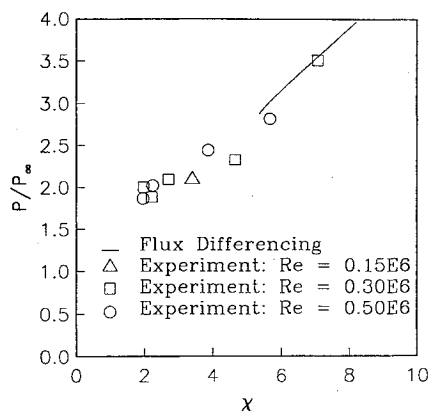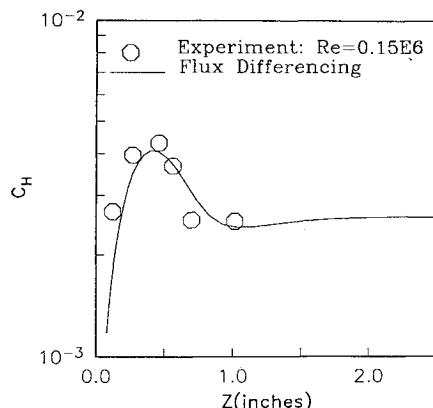
a) Wall pressure at $Z = 0.125$ in.

b) Lateral variation of heat transfer at $\chi = 8.3$

Fig. 3   Hypersonic corner flow validation.

Hypersonic Corner Flow

The hypersonic laminar flow along the intersection of two mutually perpendicular flat plates at freestream Mach number of 12 and an altitude of 100,000 ft was calculated using the calorically perfect and thermally perfect air EOS formulations. Both the central-difference and second-order upwinding approaches were used. The length of the plates is taken to be 12 in. while the widths of the plates are both taken to be 2.5 in. At this altitude the freestream temperature and pressure are $418.790°R$ and 23.085 psf, resulting in a Reynolds number based on plate length of 1.226×10^6, allowing a laminar calculation. To highlight the real gas effects, adiabatic wall boundary conditions are taken along the plates, while grid line extrapolation is taken at the outflow and lateral boundaries. Although the application of adiabatic wall boundary conditions results in unrealistically high wall temperatures, it is an extreme test of the code's robustness and the installation of the real gas effects. Since the thermally perfect EOS formulation allows for a variation in the fluid specific heats while the calorically perfect formulation does not, the difference in wall temperatures between these formulations should be readily apparent. Grid stretchings identical to that used in the validation case are used for this computation.

Figure 4 illustrates the mutual interactions of the plate boundary layers and embedded leading-edge shock structure and the downstream growth of the interaction region by showing axial velocity contours in planes perpendicular to the plates at different downstream axial locations. Figure 5 shows the predicted lateral variation of wall temperature approximately 6 in. downstream of the leading edges for both the calorically perfect and thermally perfect equations of state for both the central-difference and upwinded discretizations. This figure shows that the lateral location of the peak wall temper-

ature is predicted to be the same for each EOS formulation and each differencing scheme, although the central-difference scheme consistently predicts lower peak temperatures. This figure also shows that the wall temperature in the noninteractive region computed by the central-difference scheme is lower than that computed by the upwind scheme. The noninteractive region of the corner flowfield is far enough downstream of the leading edge so that the leading-edge effects of the primary plate are absent and far enough laterally from the corner so that the opposing plate leading-edge shock effects are also absent. This difference in computed noninteractive wall temperatures indicates that the upwinding scheme appears to be more diffusive than the central-difference scheme. This figure shows the marked reduction in wall temperature by using the chemically frozen air equation of state, which in essence allows for variation of the specific heats.

Differences between results of the two differencing schemes are apparent from a detailed examination of cross-stream contours of density and cross-stream velocity vector plots. Figure 6 compares contour plots of density from both the central-difference and upwinded discretization schemes using the chemically frozen air equation of state. These density contours are taken in a plane perpendicular to the freestream at a distance approximately 3.5 in. from the leading edge of the plates. The central-differencing results, shown in Fig. 6a,
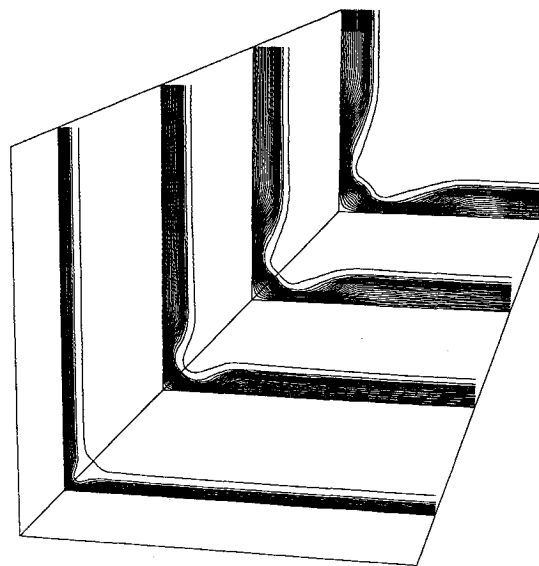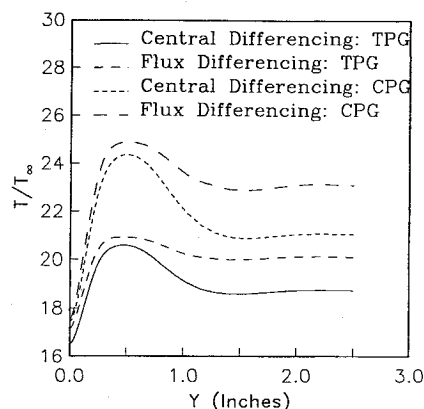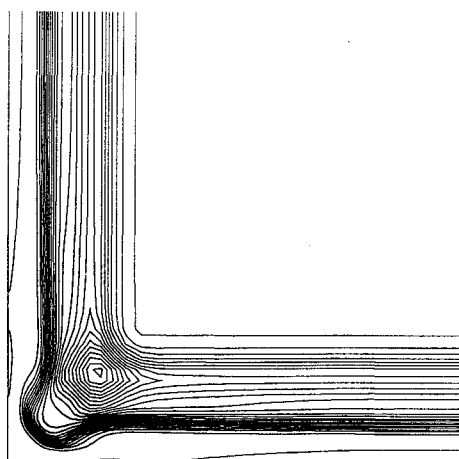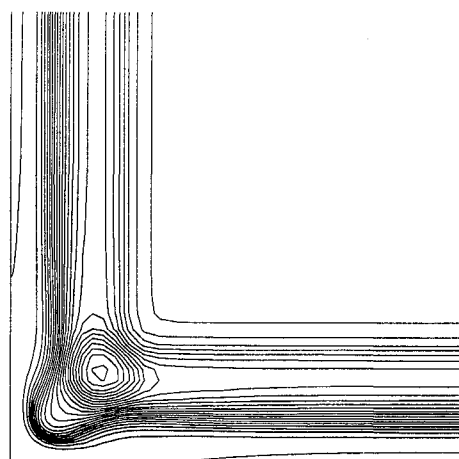

Fig. 4   Corner flowfield axial velocity contours.


Fig. 5   Lateral wall temperature variation: $X = 5.8$ in.

a) Central-differencing scheme
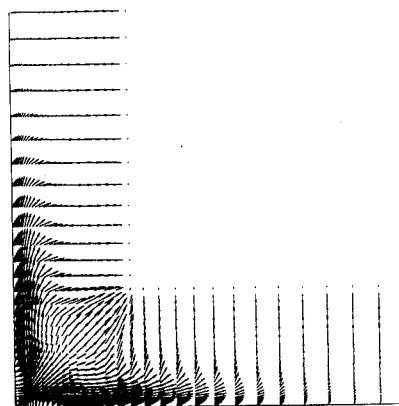

b) Flux-differencing scheme

Fig. 6   Density contours: $X = 3.5$ in.

a) Central-differencing scheme

b) Flux-differencing scheme

Fig. 7   Cross-stream velocity vectors: $X = 3.5$ in.

indicate a merging of the leading-edge shock and the plate boundary layer and an oscillatory shock/shock interaction region. The upwinded results, in Fig. 6b, indicate a more clearly defined and separate leading-edge shock and boundary layer and a cleaner shock/shock interaction. These subtle differences between the two discretization schemes are contrasted by rather different results in the cross-stream velocity field, which is shown in Fig. 7. The central-difference results, in Fig. 7a, show the beginning of a region of cross-stream separation, which results in the downstream development of a weak vortical flow just inboard of the embedded shock. The upwinded results, in Fig. 7b, indicate a much weaker cross-stream separation, resulting in a very weak vortical flow just inboard of the embedded shock. The upwinded results, in Fig. 7b, indicate a much weaker cross-stream separation, resulting in a very weak vortical flow downstream. If the upwinding scheme is indeed more dissipative than the central-difference scheme, as is indicated in the adiabatic wall temperatures, then it is possible that this vortical flow is induced by the numerical dissipation. This finding of numerically induced vortical flow has been previously investigated in detail for conical solutions to the Euler equations for flow over a delta wing.[27] The results of that study indicated that the existence and strength of the computed cross-stream vortical flow on the lee side of a blunt-tip delta wing was sensitive to the level of the second- and fourth-order dissipation coefficients. This study indicated that with lower numerical dissipation, the vortical flow disappears. Other computational results have indicated the existence of a vortical structure in corner flowfields, but the findings here
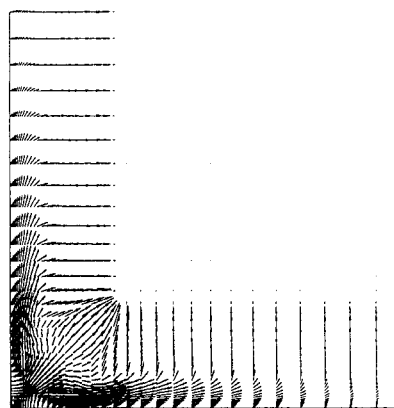
indicate that the strength is influenced by the level and type of numerical dissipation. Computations in Ref. 29 also show the differences between using different numerical flux functions for the convective terms in Navier-Stokes computations, indicating that Roe's linearized Riemann solver is the least dissipative. Clearly, more detailed experimental data and more refined numerical experiments using more accurate and less dissipative schemes are necessary to confidently predict the evolution and behavior of the corner induced vortical flow.

The relative efficiency using the generalized equation of state can be shown by comparing the processing rate per iteration of the different methods and by comparing convergence rates. All of the computations were made on a CRAY-YMP using the cft77 complier. The central-difference computations for the calorically perfect formulation and the thermally perfect formulation took 2.4575×10^{-5} and 2.7672×10^{-5} s/iteration/grid point, respectively. This represents a 12.6% increase in computing time to include the generalized equation of state. The second-order upwinding computations for the calorically perfect and thermally perfect formulations took 3.0829×10^{-5} and 3.5453×10^{-5} s/iteration/grid point, respectively. This represents a 15% increase in computing time to include the generalized equation of state in the upwinding scheme. These processing rates also indicate that the addition of the second-order upwinding scheme was made at a cost of approximately 25% over that of the central-differencing scheme. Figure 8 shows the convergence histories for this test case by plotting the L_2 norm of the flux variable corrections. This figure shows that the central-difference convergence rate is unaffected by the EOS, whereas the flux-differencing approach is slightly affected. Since the flux-differencing approach interpolates fluxes, which are not smooth
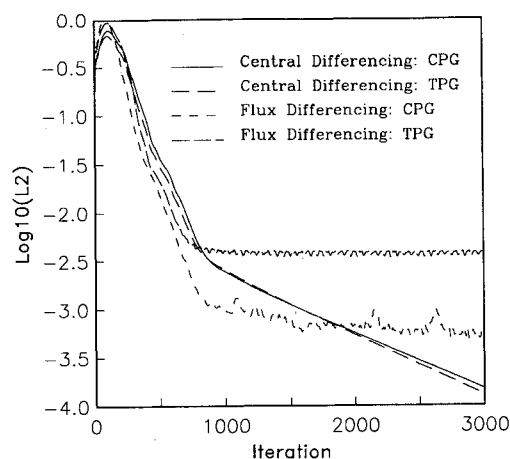
Fig. 8 Convergence histories.

interpolants, the residual stalls after a drop in two to three orders of magnitude. Future work should compare results shown here with those obtained from a MUSCL-type differencing scheme that uses Roe's linearized Riemann solver, as well as perform a detailed grid refinement study for all of the differencing schemes. Since the MUSCL differencing approach interpolates primitives (a smoother interpolant), and the Roe scheme has been shown to be the least dissipative[29] of the current upwinding schemes, more light could be shed on the structure of the hypersonic corner flowfield.

Summary and Conclusions

An efficient method to account for single stream, chemically frozen real gas effects in general three-dimensional Navier-Stokes computations has been presented. This method specified the fluid pressure, temperature, laminar viscosity, and thermal conductivity as explicit functions of the density and internal energy, which are simply related to the flux variables. By having an explicitly specified equation of state (EOS), no subiterations were required to deduce the pressure and temperature from the flux variables. The EOS approach was demonstrated by generating an equation of state for air under the assumption that it is thermally perfect, to allow for the variation of fluid specific heats with temperature. The EOSs were made available to the solver as statement functions, which allows a previously vectorized code to maintain its same basic structure and efficiency and allows different EOSs to be easily supplied to the code.

The flexibility of the EOS approach was demonstrated by including real gas effects in both the implicit and explicit portions of the numerical scheme. Since derivatives of the pressure with respect to the flux variables are immediately available from the EOS, they are included in the implicit portion of the scheme without any additional assumptions. The central-difference scheme with first and third difference dissipation originally present in the code was easily modified with the EOS formulation. A second-order, TVD upwinding scheme was then added to the solver, which was also readily modified using the EOS approach. The extension to upwinding was then favorably validated against experimental data from a hypersonic corner flow experiment.

To test the installation of real gas effects, and to compare the discretization schemes, a hypersonic corner flowfield was computed with and without the EOS. Marked differences in wall temperatures were noted between the calorically perfect and thermally perfect formulations, as well as significant differences in flow structure between the central-difference and upwinding schemes. Relative efficiencies between the calorically perfect and thermally perfect gas formulations were made by comparing processing rates and convergence histories. These comparisons indicated that by using the EOS for-

mulation the processing and convergence rates are only marginally degraded.

Appendix: Frozen Air Equation of State

The following shows the equation of state fits generated for chemically frozen air using the thermodynamic and transport data accessed by the CEC program. The supplied curve fit functions and arguments have been nondimensionalized by the following:

$$p_\infty = 101325.0 \ N/m^2 \tag{A1a}$$

$$T_\infty = 300.0 \ K \tag{A1b}$$

$$\rho_\infty = 1.17196272 \ kg/m^3 \tag{A1c}$$

$$e_\infty = 8.64571924 \times 10^4 \ m^2/s^2 \tag{A1d}$$

$$\mu_\infty = 180.16133 \ \mu P \tag{A1e}$$

$$\lambda_\infty = 12.619813 \ \mu W/cmK \tag{A1f}$$

The EOS functions for pressure, temperature, laminar viscosity, and thermal conductivity are

$$p(\rho,e) = a_1 e + a_2 \rho e + a_3 + a_4 \rho e^2 + a_5 \rho e^3 + a_6 \rho e^4 + a_7 \rho^2 e^3$$
$$+ a_8 \rho^2 e^4 + a_9 \rho e^5 + a_{10} \rho^2 e^5 + a_{11} \rho^2 e^6 + a_{12} \rho e^6 + a_{13} \rho^2 e^7$$
$$+ a_{14} \rho e^7 \tag{A2}$$

$$T(\rho,e) = b_1 e/\rho + b_2 e + b_3/\rho + b_4 e^2 + b_5 e^3 + b_6 e^4$$
$$+ b_7 \rho e^3 + b_8 \rho e^4 + b_9 e^5 + b_{10} \rho e^5 + b_{11} \rho e^6 + b_{12} e^6$$
$$+ b_{13} \rho e^7 + b_{14} e^7 \tag{A3}$$

$$\mu(T) = c_1 + c_2 T^{1/2} + c_3 T + c_4 T^{3/2} + c_5 T^2 + c_6 T^{5/2} \tag{A4}$$

$$\lambda(T) = d_1 + d_2 T^{1/2} + d_3 T + d_4 T^{3/2} + d_5 T^2 + d_6 T^{5/2} \tag{A5}$$

The EOS coefficients a_n, b_n, and d_n are shown in Table A1 and A2.

Table A1   Frozen air EOS fit coefficients for pressure and temperature

n	a_n	b_n
1	$-1.64184011 \times 10^{-08}$	$-4.66744619 \times 10^{-11}$
2	$+4.25555113 \times 10^{-01}$	$+4.11592537 \times 10^{-01}$
3	$+2.87728820 \times 10^{-06}$	$+9.27096790 \times 10^{-09}$
4	$-6.01056836 \times 10^{-03}$	$-4.76679827 \times 10^{-03}$
5	$+1.16745176 \times 10^{-04}$	$+8.29280665 \times 10^{-05}$
6	$-1.18673130 \times 10^{-06}$	$-7.78921374 \times 10^{-07}$
7	$+1.68428888 \times 10^{-07}$	$+1.35065409 \times 10^{-08}$
8	$-4.49056339 \times 10^{-09}$	$-3.13912759 \times 10^{-10}$
9	$+6.28302532 \times 10^{-09}$	$+3.84665192 \times 10^{-09}$
10	$+4.16636684 \times 10^{-11}$	$+2.65689892 \times 10^{-12}$
11	$-1.62288924 \times 10^{-13}$	$-9.73342645 \times 10^{-15}$
12	$-1.66714128 \times 10^{-11}$	$-9.60514023 \times 10^{-12}$
13	$+2.26513998 \times 10^{-16}$	$+1.30418711 \times 10^{-17}$
14	$+1.75501828 \times 10^{-14}$	$+9.61090540 \times 10^{-15}$

Table A2   Frozen air EOS fit coefficients for laminar viscosity and thermal conductivity

n	c_n	d_n
1	$-5.65406343 \times 10^{-04}$	$+1.31392583 \times 10^{-01}$
2	$+6.69279456 \times 10^{-01}$	$+8.37926287 \times 10^{-03}$
3	$+5.21149933 \times 10^{-01}$	$+1.15344608 \times 10^{-00}$
4	$-1.21977866 \times 10^{-01}$	$-2.58670568 \times 10^{-01}$
5	$+1.59535520 \times 10^{-02}$	$+3.15793268 \times 10^{-02}$
6	$-6.81970909 \times 10^{-04}$	$-1.33315276 \times 10^{-03}$

References

[1]Pulliam, T. H., and Steger, J. L., "Implicit Finite-Difference Simulations of Three-Dimensional Compressible Flow," *AIAA Journal*, Vol. 18, No. 2, 1980, pp. 159–167.

[2]Beam, R., and Warming, R. F., "An Implicit Finite-Difference Algorithm for Hyperbolic Systems in Conservation-Law Form," *Journal of Computational Physics*, Vol. 22, No. 1, 1976, pp. 87–110.

[3]Pulliam, T. H., "Euler and Thin Layer Navier-Stokes Codes: ARC2D,ARC3D," *Notes for Computational Fluid Dynamics User's Workshop*, Univ. of Tennessee Space Institute, Tullahoma, TN, UTSI Pub. E02-4005-023-84, March 1984, pp. 15.1–15.85.

[4]Cooper, G. K., "The PARC Code: Theory and Usage," Arnold Engineering Development Center, Tullahoma, TN, AEDC-TR-87-24, Oct. 1987.

[5]Coirier, W. J., "High Speed Corner and Gap-Seal Calculations using an LU Scheme," AIAA Paper 89-2669, July 1989.

[6]Jameson, A., and Turkel, E., "Implicit Schemes and LU Decompositions," *Mathematics of Computation*, Vol. 37, No. 156, 1981, pp. 385–397.

[7]Jameson, A., and Yoon, S., "LU Implicit Schemes with Multiple Grids for the Euler Equations," AIAA Paper 86-0105, Jan. 1986.

[8]Shuen, J. S., and Yoon, S., "Numerical Study of Chemically Reacting Flows Using an LU Scheme," AIAA Paper 88-0436, Jan. 1988.

[9]Yu, S. T., Tsai, Y. L., and Shuen, J. S., "Three-Dimensional Calculation of Supersonic Reacting Flows Using an LU Scheme," AIAA Paper 89-0391, Jan. 1989.

[10]Liou, M. S., and Hsu, A. T., "A Time Accurate Finite Volume High Resolution Scheme for Three Dimensional Navier-Stokes Equations," AIAA Paper 89-1994, June 1989.

[11]Van Leer, B., "Flux-Vector Splitting for the Euler Equations," *Lecture Notes in Physics*, Vol. 170, Springer-Verlag, Berlin, 1982, pp. 507–512.

[12]Mani, M. and Tiwari, S. N., "Investigation of Two-Dimensional Chemically Reacting and Radiating Supersonic Channel Flows," AIAA Paper 88-0462, Jan. 1988.

[13]Yu, S. T., McBride, B. J., Hsieh, K. C., and Shuen, J. S., "Numerical Simulation of Hypersonic Inlet Flows with Equilibrium or Finite Rate Chemistry," AIAA Paper 88-0273, Jan. 1988.

[14]Shuen, J. S., and Liou, M. S., "Flux Splitting Algorithms for Two-Dimensional Viscous Flows with Finite-Rate Chemistry," AIAA Paper 89-0388, Jan. 1989.

[15]Liou, M. S., Van Leer, B., and Shuen, J. S., "Splitting of Inviscid Fluxes for Real Gases," *Journal of Computational Physics*, Vol. 87, No. 1, March 1990, pp. 1–24.

[16]Liou, M. F., "Three Dimensional PNS Solutions of Hypersonic Internal Flows with Equilibrium Chemistry," AIAA Paper 89-0002, Jan. 1989.

[17]Gordon, S., and McBride, B. J., "Computer Program for the Calculation of Complex Equilibrium Compositions, Rocket Performance, Incident and Reflected Shocks, and Chapman-Jouget Detonations," NASA SP-273 Interim Revision, 1976.

[18]Gordon, S., McBride, B. J., and Zeleznik, F. J., "Computer Program for Calculation of Complex Chemical Equilibrium Compositions and Applications Supplement I—Transport Properties," NASA TM-86885, Oct. 1984.

[19]Yu, S. T., and McBride, B. J., "Numerical Simulation of Hypersonic Inlet Flows with Equilibrium or Finite Rate Chemistry," AIAA Paper 88-0273, Jan. 1988.

[20]National Bureau of Standards (U.S.) Circ. 564, 1955.

[21]Yoon, S., and Jameson, A., "Lower-Upper Implicit Scheme for High-Speed Inlet Analysis," *AIAA Journal*, Vol. 25, No. 8, 1987, pp. 1052, 1053.

[22]Yoon, S., and Jameson, A., "An LU-SSOR Scheme for the Euler and Navier-Stokes Equations," AIAA Paper 87-0600, Jan. 1987.

[23]Park, C., and Yoon, S., "Calculation of Real-Gas Effects on Blunt-Body Trim Angles," AIAA Paper 89-0685, Jan. 1989.

[24]Yoon, S., and Kwak, D., "Artificial Dissipation Models for Hypersonic External Flows," AIAA Paper 88-3708, July 1988.

[25]Steinetz, B. M., DellaCorte, C., and Sirocky, P., "On the Development of Hypersonic Engine Seals," NASA TP-2854, Dec. 1988.

[26]Cresci, R. J., "Hypersonic Flow Along Two Intersecting Planes," Air Force Office of Scientific Research, Farmingdale, NY, AFOSR 66-0500, March 1966.

[27]Kandil, O. A., and Chuang, A. H., "Influence of Numerical Dissipation on Computational Euler Equations for Vortex-Dominated Flows," *AIAA Journal*, Vol. 25, No. 11, 1987, pp. 1426–1434.

[28]Coirier, W. J., "Efficient Real Gas Navier-Stokes Computations of High Speed Flows Using an LU Scheme," AIAA Paper 90-0391, Jan. 1990.

[29]Van Leer, B., Thomas, J. L., Roe, P. L., and Newsome, R. W., "A Comparison of Numerical Flux Formulas for the Euler and Navier-Stokes Equations," AIAA 87-1104, 1987.